

Received July 23, 2019, accepted August 1, 2019, date of publication August 7, 2019, date of current version August 19, 2019.

Digital Object Identifier 10.1109/ACCESS.2019.2933695

# Theoretical Study on Control Strategy of Grid-Connected High Voltage Ride Through in Doubly-Fed Wind Farm

XINYU LIU, XIANWEI LI<sup>✉</sup>, AND DONGHONG JIAO

School of Electric Power, North China University of Water Resource and Electric Power, Zhengzhou 450011, China

Corresponding author: Xinyu Liu (lxy22101@163.com)

This work was supported in part by the Henan Science and Technology Research Project under Grant 162102210078, in part by the Henan Key Youth Teacher Research Project under Grant 2016GGJS-074, and in part by the Henan Provincial Department of Education Science and Technology Research Key Project under Grant 14B413005.

**ABSTRACT** Aiming at the problem of high voltage disconnection when doubly-fed wind farms are merged into weak power grids, this paper researches the theory of rotor excitation control and proposed an additional control model of DFIG grid-connected rotor flux based on structure decentralization theory. In this model, the high voltage ride-through capability for grid-connected wind farms is enhanced by designing the d-axis and q-axis adaptive terminal sliding mode controllers of the synchronous rotating coordinate system. Using the simulation software of MATLAB/Simulink, this paper established a simulation model of wind farm high voltage ride through composed of 2MW doubly fed wind turbines and carried out the off-line simulation of the whole process of high voltage traversing. Real-time simulation experiment of high voltage ride-through was also conducted on a self-developed real-time simulation platform for grid-connected doubly-fed wind farms. Real-time simulation results prove the accuracy of theoretical and offline simulation analysis and the feasibility of control strategy.

**INDEX TERMS** Doubly-fed wind farm, high voltage ride through, structure decentralization, terminal sliding mode control.

## I. INTRODUCTION

Most of China's large wind farms are located in remote areas, away from the load center of the power system, and they are typical weak grid [1], [2]. The grid connection of high proportion wind farms raises questions about the safe and stable operation of power systems [3]–[6]. In order to deal with these problems, many countries such as the United States and China have introduced strict wind power grid-connected regulations [7], [8], they are also required that during grid faults and voltage fluctuations, the wind farm must quickly emit a certain amount of dynamic reactive power to enhance its low voltage or high voltage ride through capability. Regarding the low voltage ride-through problem of wind power grid-connected, domestic and foreign scholars have carried out a lot of theoretical research and practice work, and made great progress [9]–[14], and the

low voltage ride-through technology is improving day by day. However, after wind farm achieves low voltage ride through, due to the limitation of the switching speed of the reactive power compensation device in the power system and the local reactive power is excessive, which causes the instantaneous high voltage fault of the system and the wind turbine to be disconnected again, this directly affects the safe and stable operation of the power system. Therefore, in order to meet the requirements of wind power connection to the grid, wind turbines not only require low voltage ride through capability, but also require high voltage ride through capability.

At present, although some progress has been made in the research on high voltage traversal of wind farms, these results show their effectiveness in some aspects of wind power grid-connected voltage and high voltage traversal, and it is difficult to guarantee its versatility. Literature [15] discusses methods to overcome the challenges of real-time simulation of wind systems, characterized by their complexity and

The associate editor coordinating the review of this manuscript and approving it for publication was Canbing Li.

high-frequency switching. A hybrid flow-battery supercapacitor energy storage system (ESS) is studied by real-time HIL simulation. The simulation results of the detailed wind system model show that the hybrid ESS has a lower battery cost, higher battery longevity, and improved overall efficiency over its reference ESS. Literature [16] presents an energy function-based optimal control strategy for output stabilization of integrated doubly fed induction generator (DFIG)-flywheel energy storage architecture. It can keep the grid power isolated from wind power output and voltage fluctuations and thus enabling increased penetration of wind energy resources. This control strategy is proposed for maximum energy transfer from wind farm during normal operation and to improve DFIG low voltage ride through characteristics. Literature [17] examines the impact of an LVRT scheme on grid-integrated doubly fed induction generator (DFIG)-based wind turbines which are represented with new stator-damping resistor unit (SDRU) and rotor current control (RCC). The results show that the system became stable in a short time when the SDRU and RCC were incorporated with the stator and rotor electro-motor-force models. Literature [18] presents dynamic behavior and simulation results in a stand-alone hybrid power generation system of wind turbine, micro-turbine, solar array and battery storage. The integration of a wind turbine, a solar array, a microturbine, and a battery storage which work together in order to provide sufficient electric energy supply to satisfy the stand-alone load demands at all times was proposed and considered. Comparison of proposed method with fuzzy logic and PID controllers indicates that operation of the proposed adaptive controller is the best. Literature [19] discusses the Low Voltage Ride Through (LVRT) capability was enhanced by a Demagnetization Current Controller (DCC) for the purpose of transient analysis. Parameters for the DFIG including output voltage, speed, electrical torque variations and d-q axis rotor-stator current variations in addition to a 34.5kV bus voltage were examined. It was found that in the DFIG model the system became stable in a short time when using the DCC. Literature [20] deals with the coordinated control of rotor- and grid-side converters in wind turbines with doubly fed induction generators (DFIGs) to improve the low-voltage ride-through capability. A non-linear control scheme applied to the grid-side converter is proposed, which stabilizes the internal dynamics and limits the dc-link voltage fluctuations during the fault. The proposed ride-through approaches limit the peak values of rotor current and dc-link voltage at the instants of occurring and clearing the fault. They also limit the oscillations of electromagnetic torque, and consequently, improve the DFIG voltage dip behavior. In the literature [21], the passive Low voltage Ride Through (LVRT) capability method as well as the active LVRT capability method were developed for the purpose of transient analysis of the DFIG. Simulation analysis found that the system became stable in a short time when the active LVRT was incorporated into the reduced order DFIG model. Literature [22] proposes a competent and effective scheme to enhance the ride-through capability of DFIG-based

wind turbines under unbalanced voltage dip conditions. The proposed method is realized through joint use of the rotor-side converter control and a three-phase stator damping resistor (SDR) placed in series with the stator windings. The proposed ride-through approach limits the peak values of the rotor inrush current, electromagnetic torque and DFIG transient response at the times of occurrence and clearing the fault. It also suppresses fluctuation of the electromagnetic torque and DFIG transient response appeared during unbalanced voltage dips due to negative sequence component. Literature [23] discusses the transient stability analyses of the DFIG with and without supercapacitor as well as positive-negative-sequence dynamic modeling (PNSDM). It was found that the DFIG-based wind farm became stable within a short time using the PNSDM and supercapacitor. Literature [24] proposes the use of doubly-fed induction generator based low-voltage-ride-through scheme including crowbar, rotor-side converter, grid-side converter and power system stabilizers. The simulation results that the proposed control scheme improves the operation of doubly-fed induction generator during faults. The transient stability and damping of the electro-mechanical oscillations of a grid-connected doubly-fed induction generator is obtained. Literature [25] proposes a novel scheme for enhancing the fault ride-through (FRT) capability of Doubly Fed Induction Generator (DFIG). This coordinated control aids rapid recovery of terminal voltage at the clearance of severe grid fault. Literature [26] proposes a control system, for crowbar protection and voltage support, for wind turbines equipped with doubly fed induction generator. The simulation results highlights that the proposed control improves the coordination between grid side converter, rotor side converter, and crowbar protection. Literature [27] presents a control strategy for wind turbines to enhance their fault ride-through capability. The controller design is based on pitch controlled variable speed wind turbine equipped with doubly-fed induction generator (DFIG). It is shown that the combined mechanical and electrical controller design significantly improves the wind turbine fault ride-through capability.

According to the analysis of the above literature, the domestic and foreign scholars have proposed many control strategies and control algorithms for the high voltage ride-through of wind turbines. However, there are few mentions on the rapidity of reactive power regulation when an overvoltage fault occurs, and the millisecond-level reactive power control technology is the key to solving the system over-voltage problem. This paper focuses on the basic grid-connected operation model of DFIG, fully exploits the dynamic characteristics of the rotor flux linkage and its effect on the reactive power of the DFIG output, an adaptive terminal sliding mode additional control strategy for the rotor flux linkage is proposed, which enables the wind farm to quickly absorb excess reactive power during the grid fault to reduce the instantaneous high voltage at the grid bus and improve the quality and stability of the grid-connected voltage of the doubly-fed wind farm.

## II. DFIG STRUCTURE DECENTRALIZED DYNAMIC MATHEMATICAL MODEL.

The equivalent mathematical model of DFIG in the synchronous rotation d, q coordinate system is as follows.

The stator and rotor voltage equation are as follows,

$$\begin{cases} u_{ds} = -R_s i_{ds} + \dot{\varphi}_{ds} - \omega_1 \varphi_{qs} \\ u_{qs} = -R_s i_{qs} + \dot{\varphi}_{qs} + \omega_1 \varphi_{ds} \\ u_{dr} = R_r i_{dr} + \dot{\varphi}_{dr} - \omega_s \varphi_{qr} \\ u_{qr} = R_r i_{qr} + \dot{\varphi}_{qr} + \omega_s \varphi_{dr} \end{cases} \quad (1)$$

The stator and rotor flux equation are as follows,

$$\begin{cases} \varphi_{ds} = -L_s i_{ds} + L_m i_{dr} \\ \varphi_{qs} = -L_s i_{qs} + L_m i_{qr} \\ \varphi_{dr} = -L_r i_{dr} + L_m i_{ds} \\ \varphi_{qr} = -L_r i_{qr} + L_m i_{qs} \end{cases} \quad (2)$$

The power output equation of the stator end is as follows,

$$\begin{cases} P_s = u_{ds} i_{ds} + u_{qs} i_{qs} \\ Q_s = u_{qs} i_{ds} - u_{ds} i_{qs} \end{cases} \quad (3)$$

where  $L_m$  is the mutual inductance;  $L_s$  and  $L_r$  are the stator and rotor inductance;  $R_s$  and  $R_r$  are the stator and rotor inductance;  $\omega_1$  and  $\omega_s$  are the synchronous and rotor angular speed;  $u_{ds}$ ,  $u_{qs}$ ,  $u_{dr}$  and  $u_{qr}$  are the d, q components of the stator and rotor voltage respectively;  $i_{ds}$ ,  $i_{qs}$ ,  $i_{dr}$  and  $i_{qr}$  are the d, q components of the stator and rotor current respectively;  $\varphi_{ds}$ ,  $\varphi_{qs}$ ,  $\varphi_{dr}$ ,  $\varphi_{qr}$  are the d, q components of the stator and rotor flux respectively;  $P_s$  and  $Q_s$  are the stator active and reactive power.

When the grid voltage is symmetrically operated, orienting the stator flux  $\varphi$  on the d-axis of the synchronously rotating d-q coordinate system, and the magnetic fluxes on the d and q axes are:  $\varphi_{ds} = \varphi_s$ ,  $\varphi_{qs} = 0$ . The induced electromotive force of DFIG is approximately equal to the stator voltage, that is,  $u_{ds} = 0$ ,  $u_{qs} = u_s$ ;  $u_{qs}$  is the amplitude of the vector of the stator voltage. When the stator is incorporated into the ideal grid,  $u_{qs}$  is equal in amplitude to the grid voltage. The resistance of stator winding is much smaller than the reactance of stator winding, so the influence of stator resistance can be ignored. At this point the stator flux and current equation are obtained,

$$\begin{cases} \varphi_{ds} = \frac{u_{qs}}{\omega_1} = \frac{u_s}{\omega_1} \\ \dot{\varphi}_{ds} = 0 \end{cases} \quad (4)$$

$$\begin{cases} i_{ds} = \frac{L_m i_{dr} - \varphi_{ds}}{L_s} \\ i_{qs} = \frac{L_m i_{qr}}{L_s} \end{cases} \quad (5)$$

When the grid fluctuates, DFIG is in an unstable state, and the DFIG stator voltage and stator flux linkage are not constant. Therefore, when the DFIG transient operation is analyzed, the change of the flux linkage cannot be ignored. The flux linkage change cannot be abruptly changed, and the

stator flux linkage change causes the stator excitation current to also change. At this time,  $\dot{\varphi}_{ds} \neq 0$  in the formula (4) takes the above into consideration.

Substituting equation (5) into equations (2) and (1) to obtain,

$$\begin{cases} \dot{\varphi}_{dr} = -\frac{R_r L_s}{L_m^2 - L_r L_s} \varphi_{dr} + \omega_s \varphi_{qr} - \frac{R_r L_m u_s}{\omega_1 (L_m^2 - L_r L_s)} + u_{dr} \\ \dot{\varphi}_{qr} = -\frac{R_r L_s}{L_m^2 - L_r L_s} \varphi_{qr} - \omega_s \varphi_{dr} + u_{qr} \end{cases} \quad (6)$$

Substituting equation (5) into equations (3) and (2) to obtain the active power and reactive power equation,

$$\begin{cases} P_s = \frac{u_s L_m}{L_s} i_{qr} \\ = \frac{u_s L_m}{L_m^2 - L_r L_s} \varphi_{qr} \\ Q_s = \frac{u_s L_m}{L_s} i_{dr} - \frac{u_s}{L_s} \varphi_{ds} \\ = \frac{u_s L_m}{L_m^2 - L_r L_s} \varphi_{dr} + \frac{(L_m^2 - L_s L_m + L_r L_s^2) u_s}{L_s (L_m^2 - L_r L_s)} \varphi_{ds} \end{cases} \quad (7)$$

The grid side converter is a converter near the grid side of the back-to-back converter, which functions to regulate the power factor and maintain the constant voltage of the bus. The formula is as follows,

$$\begin{cases} E_a = U_m \cos(\omega t) \\ E_b = U_m \cos\left(\omega t - \frac{2\pi}{3}\right) \\ E_c = U_m \cos\left(\omega t + \frac{2\pi}{3}\right) \end{cases} \quad (8)$$

where  $E_k$  ( $k = a, b, c$ ) is power voltage,  $U_m$  is peak voltage.

In a three-phase synchronous rotating coordinate system, the mathematical model of the grid-side converter can be described as,

$$\begin{cases} L_g \frac{di_{gd}}{dt} = E_d - R_g i_{gd} + \omega_g L_g i_{gq} - \mu_{gd} u_{dc} \\ L_g \frac{di_{gq}}{dt} = E_q - R_g i_{gq} - \omega_g L_g i_{gd} - \mu_{gq} u_{dc} \\ L_g \frac{du_{dc}}{dt} = i_{dc} - i_L = (\mu_{gd} i_{gd} + \mu_{gq} i_{gq}) - i_L \end{cases} \quad (9)$$

where  $R_g$  is the resistance,  $L_g$  is the inductance,  $u_{gd}$  and  $u_{gq}$  are d, q-axis components of grid electromotive force,  $i_{gd}$  and  $i_{gq}$  are active current and reactive current of grid-side converter,  $i_L$  is load current on the DC side,  $\omega_g$  is angular velocity of the grid voltage,  $i_{dc}$  is q-axis component of three-phase VSR input current vector.

Orienting the d-axis of the synchronous rotating coordinate system in the direction of the grid voltage vector,  $u_{gd} = u_g$ ,  $u_{gq} = 0$ .

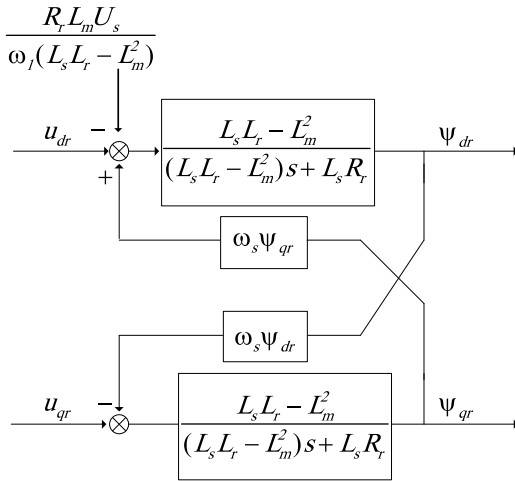


FIGURE 1. Diagram of the relationship between applied voltage and flux linkage of DFIG rotor.

The active power and reactive power output from the grid-side converter to the grid are shown in the following equation,

$$\begin{cases} P_g = -\frac{3}{2}u_g i_{gd} \\ Q_g = \frac{3}{2}u_g i_{gq} \end{cases} \quad (10)$$

where  $P_g$  is active power,  $Q_g$  is reactive power;  $u_g$  is power voltage.

### III. DFIG ADDITIONAL ROTOR MAGNETIC LINKAGE CONTROL DESIGN

During the voltage surge caused by a grid failure, the wind farm emits reactive power to reduce the fluctuation of the grid voltage. The feasibility of this approach must have two prerequisites: One is the rapidity of the reactive power of the wind farm, and the other is whether the rotor will over-current when the wind farm emits reactive power. For the first precondition, it is known from equations (6) and (7) that the reactive power of the doubly-fed wind farm depends on the d-axis component of the rotor flux linkage, while the d-axis component of the rotor flux linkage is controlled by the d-axis exciting voltage. Its time constant is  $\tau = \frac{L_m^2 - L_r L_s}{R_r L_s}$ , the time is generally 8~15ms. Therefore, the reactive power adjustment time of the doubly-fed wind farm is in milliseconds, which is almost equal to the reactive power compensation speed of the static var compensator. For the second precondition, the general researcher believes that increasing the reactive output of the wind turbine will significantly increase the exciting current of the rotor and impose an additional burden on the rotor-side variable-frequency drive. This understanding is appropriate for wind farms to access strong electric fields. However, when the wind farm is connected to the weak grid, the voltage of the point of combined to the grid is adjusted by the wind farm's own reactive power adjustment capability, and the exciting current of the rotor-side variable-frequency drive is not significantly increased.

It can be seen from the analysis of Fig. 1 that when the DFIG is in the grid-connected power generation operation

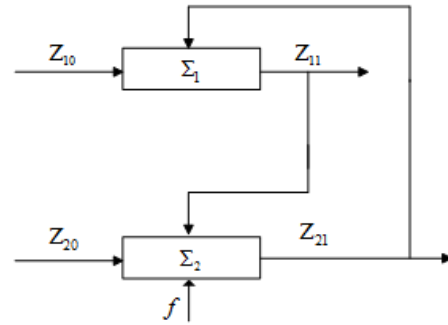


FIGURE 2. DFIG grid-connected running magnetic chain structure decentralized model.

state, the controlled output of the system is the rotor magnetic linkage  $\Psi_{dr}$  and  $\Psi_{qr}$  on doubly-fed motor, and the control inputs are the rotor voltages, which are  $u_{dr}$  and  $u_{qr}$ . The two lead a causal chain, this is defined in order as  $L_i = \{(Z_{ij-1}, Z_{ij})|j = 1, 2, i = 1, 2\}$ .

(1) DFIG rotor d-axis flux linkage  $L_1$ :  $Z_{10}$  is the rotor d-axis excitation voltage  $u_{dr}$ ;  $Z_{11}$  is the rotor d-axis flux component  $\Psi_{dr}$ ;

(2) DFIG rotor q-axis flux linkage  $L_2$ :  $Z_{20}$  is the rotor q-axis excitation voltage  $u_{qr}$ ;  $Z_{21}$  is the rotor q-axis flux component  $\Psi_{qr}$ ;

The above analysis results in a DFIG grid-connected flux linkage structure decentralized model as shown in Figure 2.

Figure 2 consists of two subsystems,  $Z_{10}$  and  $Z_{20}$  are inputs,  $Z_{11}$  and  $Z_{21}$  are outputs, and the two outputs simultaneously affect each other's subsystems. It can be seen from the figure that  $L_i$  is a simple and complete causal chain, so the inputs  $Z_{i0}$  can control the outputs  $Z_{i1}$  through the corresponding unit model. Therefore, the controllers of the two subsystems in Fig. 2 can be separately designed to realize the control of the generator rotor flux linkage.

If the component of the DFIG rotor magnetic linkage is completely adaptive to the disturbance caused by the grid fault, it can be implemented by the method of sliding mode variable structure control. In order to do this, write equation (6) into the following state space equation form,

$$\dot{Z} = AZ + BU + F \quad (11)$$

$$A = \begin{bmatrix} -\frac{L_s R_r}{L_s L_r - L_m^2} & \omega_s \\ \frac{L_s R_r}{L_s L_r - L_m^2} & -\omega_s \end{bmatrix} \quad (11-1)$$

$$B = \begin{bmatrix} 1 & 0 \\ 0 & 1 \end{bmatrix} \quad (11-2)$$

$$F = \begin{bmatrix} f \\ 0 \end{bmatrix}, \quad (11-3)$$

$$f = -\frac{R_r L_m U_s}{\omega_1 (L_s L_r - L_m^2)} \quad (11-4)$$

where  $F$  denotes the disturbance caused by the grid fault,  $Z = \begin{bmatrix} z_{11} \\ z_{21} \end{bmatrix}$  denotes state variable,  $U = \begin{bmatrix} z_{10} \\ z_{20} \end{bmatrix}$  denotes control input,  $Z_{11}$  denotes the rotor d-axis magnetic linkage which is  $\Psi_{dr}$ ,  $Z_{21}$  denotes the rotor q-axis magnetic linkage which is  $\Psi_{qr}$ ,  $Z_{10}$  denotes the rotor d-axis current control signal which is  $u_{dr}$ ,  $Z_{20}$  denotes the rotor q-axis current control signal which is  $u_{qr}$ .

It is easy to prove that the following equation is obtained,

$$\text{rank} [B F] = \text{rank} [B] = 2 \quad (12)$$

According to equation (9), we can know the sliding mode of the doubly-fed wind power generation system satisfies the necessary and sufficient conditions free from external interference [30], [31]. Therefore, the design of a suitable sliding mode controller makes the doubly-fed wind turbines completely robust to the disturbance caused by the grid fault, and its sliding mode is not affected by the grid fault.

The state variable of the system is defined as the error of the rotor q-axis flux linkage and the given value, that is  $e_d = Z_{11}^* - Z_{11}$ . According to equation (6), the error equation of the d-axis magnetic linkage of the doubly-fed induction wind turbine can be written as,

$$\dot{e}_d = -\frac{R_r L_s}{L_m^2 - L_r L_s} e_d - \omega_s z_{21} - z_{10} + F_d \quad (13)$$

where  $F_d = (\frac{L_s R_r}{L_m^2 - L_r L_s} z_{11}^* + f)$  is the disturbance caused by the grid fault.

In view of the above, the following integral sliding surface is proposed in this paper,

$$s_d = k_{pd} e_d + k_{id} \int_0^t e_d^{p/q} d\tau \quad (14)$$

where  $k_{pd}$  and  $k_{id}$  are proportionality coefficient and integral coefficient,  $k_{pd}$  and  $k_{id}$  are both larger than zero.

The proportional term is used to speed up the dynamic tracking response of the system, and the integral term is used to eliminate the steady-state error of the system. Therefore, on the PI integral sliding mode hypersurface, changing the values of  $k_{pd}$  and  $k_{id}$  can change the dynamic characteristics of the sliding surface.

According to the integral terminal sliding mode surface proposed in this paper, it is very difficult to determine the upper bound of  $F_d$  in practical control. Even if the upper bound of generalized disturbance is known, in order to ensure the robustness of the control system when the disturbance is large, the constant switching gain  $\eta_d$  of the controller is larger, which leads to serious chattering of the system. Dynamic quality and robustness cannot be guaranteed. Therefore, a sliding mode variable structure controller with adaptive switching gain is designed. Whether or not the upper bound of  $F_d$  is known, the controller can always enhance the robustness of the uncertainty. The improved switching gain equation is as follows,

$$\eta'_d = (1 + \mu(s) e^{\lambda_d \mu(s)t}) \eta_d \quad (15)$$

where  $\mu(s_d) = \text{sgn}(s_d) \text{sgn}(s'_d)$ ,  $s'_d(t) = s_d(t + \tau)$ ,  $0 < \lambda_d < 1$ ,  $\tau$  is the delay time constant.

When the system state is far from the sliding mode surface, the switching control gain  $\eta'_d$  will increase rapidly with the regular  $\eta'_d = (1 + e^{\lambda_d t}) \eta_d$ . However, when the system state moves across the sliding surface, the controller switching gain  $\eta'_d$  will gradually decrease with the regular  $\eta'_d = (1 + e^{\lambda_d t}) \eta_d$ .

According to the integral terminal sliding mode surface proposed in this paper, if the generalized perturbation term  $|F_d| < k_d$ ,  $k_d$  is constant and greater than zero, the following theorem is obtained.

*Theorem:* If the doubly-fed wind power generation grid-connected control system satisfies  $|F_d| < k_d$  and selects the integral terminal sliding mode surface of equation (11), then the adaptive switching gain  $\eta'_d$  is used to obtain the following control law,

$$z_{10} = -\frac{R_r L_s}{L_m^2 - L_r L_s} e_d - \omega_s z_{21} + \frac{k_{id}}{k_{pd}} e_d^{p/q} + \eta'_d \text{sgn}(s_d) \quad (16)$$

The d-axis magnetic error  $e$  of the DFIG can be converged to zero in a finite time, and the system is stable.

*Proof:* Firstly, the proof process of the convergence of the d-axis flux linkage error  $e$  of the doubly-fed induction wind turbine is as follows.

According to equation (14), the initial state of the integral term is set as follows as,

$$\int_{-\infty}^0 e_d^{p/q} d\tau = -\frac{k_{pq}}{k_{id}} e_{d0} \quad (17)$$

where  $e_{d0}$  denotes deviation of the initial time of the system.

Then, at time  $t=0$ , substituting equation (17) into equation (14),

$$s_d(0) = k_{pd} e_{d0} + k_{id} \int_{-\infty}^t e_d^{p/q}(\tau) d\tau = k_{pd} e_{d0} - k_{id} \frac{k_{pd}}{k_{id}} e_{d0} = 0 \quad (18)$$

Equation (18) shows that choose the appropriate initial value to make  $S_d(0) = 0$ , it is ensured that the system is on the sliding surface in the initial state to improve the robustness of the system.

It can be known from equation (14) that when the system reaches the sliding surface, there is  $\dot{s}_d = s_d = 0$ , there are equations as follows as,

$$\dot{e}_d = -\frac{k_{id}}{k_{pd}} e_d^{p/q} \quad (19)$$

The error equation of the d-axis component of the flux linkage of the doubly-fed induction wind turbine is obtained as follows,

$$\dot{e}_d \frac{1}{\frac{k_{id}}{k_{pd}} e_d^{p/q}} = -1 \quad (20)$$

Simultaneous integration on both sides of equation (20) yields the equation as follows as,

$$\int_{e_d}^0 \frac{1}{\frac{k_{id}}{k_{pd}} e_d^{p/q}} de_d = -\int_0^{\Delta t} dt \quad (21)$$

The equation for solving (21) is as follows,

$$\Delta t_d = \frac{qk_{pd}}{k_{id}(q-p)} e_d^{1-\frac{p}{q}} \quad (22)$$

Equation (22) shows that the tracking error of the magnetic linkage d-axis component of the doubly-fed induction wind turbine can converge to zero in the  $\Delta t_d$  time.

The following proves the stability of the system: Since the upper bound  $F_d$  of uncertainty  $k_d$  is unknown, there are two cases for the initial value of switching adaptive switching gain  $\eta'_d$ : One case is  $\eta'_d > k_d$ . Another case is  $\eta'_d < k_d$ . The stability of the system in these two cases is proved.

When  $\eta'_d > k_d$  and  $\eta'_d > |F_d|$  are satisfied at any time, the Lyapunov function is selected as  $V = \frac{1}{2}s_d^2$ , then,

$$\begin{aligned} \dot{V} &= s_d \dot{s}_d \\ &= s_d [k_{pd} (-\frac{R_r L_s}{L_m^2 - L_r L_s} e_d - \omega_s z_{21} - z_{10} + F_d) + k_{id} e_d^{p/q}] \\ &= s_d (-k_{pd} \frac{R_r L_s}{L_m^2 - L_r L_s} e_d - k_{pd} \omega_s z_{21} + k_{pd} \frac{R_r L_s}{L_m^2 - L_r L_s} e_d \\ &\quad + k_{pd} \omega_s z_{21} - k_{id} e_d^{p/q} - \eta'_d \text{sgn}(s_d) + k_{pd} F_d + k_{id} e_d^{p/q}) \\ &= s_d (-\eta'_d \text{sgn}(s_d) + F_d) \\ &\leq (-\eta'_d |s_d| + |F_d| |s_d|) \\ &\leq -|s_d| (\eta'_d - k_d) < 0 \end{aligned} \quad (23)$$

According to the analytical formula (23), the system always satisfies the reachable condition. Although the system may be temporarily away from the sliding mode surface, it will quickly reach the sliding mode surface under the control of the switching, thus ensuring the robust stability of the system.

When  $\eta'_d > k_d$  and  $\eta'_d > |F_d|$  are satisfied at any time, the Lyapunov function is selected as  $V = \frac{1}{2}s_q^2$ , and the following equation is obtained,

$$\begin{aligned} \dot{V} &= s_d \dot{s}_d \\ &= s_d [k_{pd} (-\frac{R_r L_s}{L_m^2 - L_r L_s} e_d - \omega_s z_{21} - z_{10} + F_d) + k_{id} e_d^{p/q}] \\ &= s_d (-k_{pd} \frac{R_r L_s}{L_m^2 - L_r L_s} e_d - k_{pd} \omega_s z_{21} + k_{pd} \frac{R_r L_s}{L_m^2 - L_r L_s} e_d \\ &\quad + k_{pd} \omega_s z_{21} - k_{id} e_d^{p/q} - \eta'_d \text{sgn}(s_d) + k_{pd} F_d + k_{id} e_d^{p/q}) \\ &= s_d (-\eta'_d \text{sgn}(s_d) + F_d) \\ &\leq (-\eta'_d |s_d| + |F_d| |s_d|) \\ &\leq -|s_d| (\eta'_d - |F_d|) \end{aligned} \quad (24)$$

In this case, due to  $\eta'_d < |F_d|$ , the condition  $-|s_d| (\eta'_d - |F_d|)$  is temporarily unsatisfiable. At the beginning, the system moves away from the direction of the sliding surface, but at the same time, the value of the adaptive switching gain  $\eta'_d$  rapidly increases under the designed control strategy. In addition, the uncertain disturbance is bounded, so after a period of time,  $\eta'_d = (1 + e_d^{\lambda_d t}) \eta_d$  will appear, and even  $\eta'_d = (1 + e_d^{\lambda_d t}) \eta_d$  will occur. At this time,  $V' = s_d \dot{s}_d < 0$  satisfies the accessibility of the sliding mode, and the system

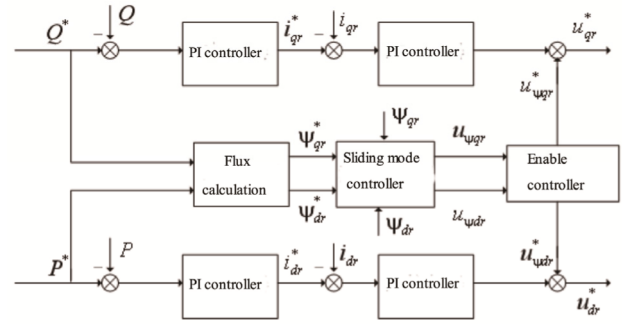


FIGURE 3. DFIG rotor flux linkage adaptive terminal sliding mode additional control block diagram.

returns to the sliding surface. It guarantees the robustness of the system.

Therefore, under the above-mentioned adaptive switching control, the system will eventually make an approaching motion across the sliding surface near the sliding surface, and it will reach a stable point within a limited time. Although there may be a large amplitude of the system crossing the sliding mode surface for the first time, as the number of crossings increases, the amplitude will gradually decay according to  $\eta'_d = (1 + e_d^{\lambda_d t}) \eta_d$  with time, and finally stabilized on the sliding surface.

Similarly, the q-axis magnetic linkage control law of the doubly-fed wind power generator is the following equation,

$$z_{20} = -\frac{R_r L_s}{L_m^2 - L_r L_s} e_q - \omega_s z_{11} + \frac{k_{iq}}{k_{pq}} e_q^{p/q} + \eta'_q \text{sgn}(s_q) \quad (25)$$

According to the control rate of the above design, the block diagram of the rotor flux linkage terminal sliding mode control of the doubly-fed induction wind turbine connected to the grid is shown in Fig. 3. The function of the enable control link in the figure is that the additional control generated by the flux-chain sliding mode controller works only when the grid fails and causes the DFIG rotor magnetic linkage to change dramatically. The additional control does not work when the system is in normal operation. The function equation used in the enable control section is as follows as,

$$\begin{cases} u_{\psi_{dr}}^* = u_{\psi_{dr}} \text{sgn}(|\psi_{dr}^* - \psi_{dr}|) \\ u_{\psi_{qr}}^* = u_{\psi_{qr}} \text{sgn}(|\psi_{qr}^* - \psi_{qr}|) \end{cases} \quad (26)$$

It can be seen from Fig. 3 that according to the given values of active and reactive power and equation (7), the rotor flux component command values  $\Psi_{qr}^*$  and  $\Psi_{dr}^*$  are calculated, and the flux linkage feedback values  $\Psi_{qr}$  and  $\Psi_{dr}$  are calculated through the real-time calculation of the flux linkage. The rotor flux linkage sliding mode controller outputs additional control signals  $u_{\psi_{dr}}^*$  and  $u_{\psi_{qr}}^*$  of the frequency converter. When the grid is disturbed due to a fault, the flux linkage additional control signal works because the flux-sliding mode controller of DFIG is robust to external disturbances, thereby causing the terminal voltage drop and rotor overcurrent are greatly weakened.

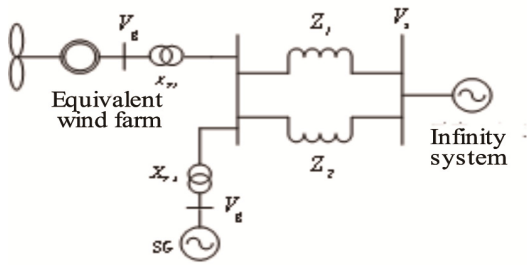


FIGURE 4. Wind power / thermal power hybrid transmission system structure.

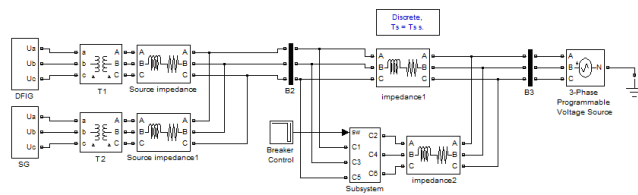


FIGURE 5. Wind power / thermal power hybrid transmission system simulation model diagram.

IV. SYSTEM OFFLINE SIMULATION AND ANALYSIS

In order to verify the effectiveness of the DFIG additional rotor flux linkage adaptive terminal sliding mode control strategy proposed in this paper, the simulation diagram of DFIG power flux linkage double closed loop control system established by Power System Toolbox of simulation software Matlab / Simulink is shown in Fig. 5. Figure 4 is its structure diagram. It should be noted that the converter in the simulation model of this chapter still uses the average voltage model. The simulation system consists of 5 doubly-fed generators and a synchronous generator model.

The main parameters are as follows:

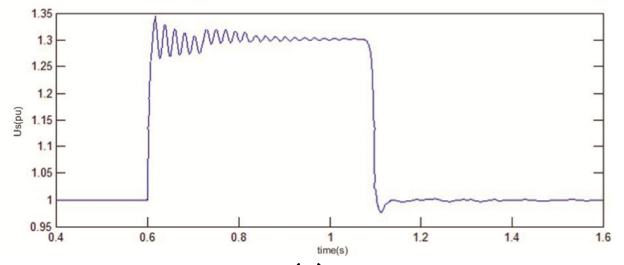
Doubly-fed wind turbine parameters: rated power is  $P_N = 2\text{MW}$ , rated voltage is  $U_N = 690\text{V}$ , Rated frequency is  $f_N = 50\text{Hz}$ , Synchronous speed is  $n_N = 1800\text{r/min}$ , Stator resistance is  $R_S = 0.008\Omega$ , Rotor resistance is  $R_r = 0.0019\Omega$ (Stator measurement), Stator inductance is  $L_S = 0.002\text{H}$ ,  $L_r = 0.0047\text{H}$ (Stator measurement), Mutual sense is  $L_m = 0.00547\text{H}$ (Stator measurement),  $R = 2.5\text{k}\Omega$ .

Synchronous motor equivalent parameters: rated power is  $P_N = 15\text{MW}$ , Rated voltage is  $U_N = 690\text{V}$ , Rated frequency is  $f_N = 50\text{Hz}$ , Synchronous speed is  $n_N = 1800\text{r/min}$ , Stator resistance is  $R_S = 0.00076\Omega$ , Rotor resistance is  $R_r = 0.000173\Omega$  (Stator measurement), Stator inductance is  $L_s = 0.012\text{H}$ ,  $L_r = 0.0047\text{H}$ (Stator measurement), Mutual sense is  $L_m = 0.00375\text{H}$ (stator calculation value),  $R = 2.5\text{k}\Omega$ .

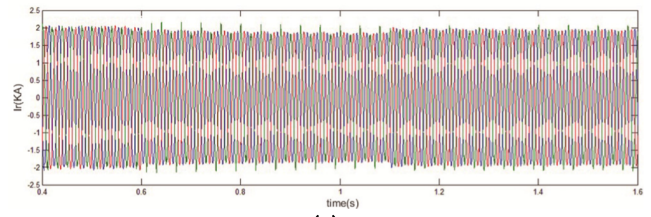
Network parameters:  $X_{T1} = X_{T2} = j52.6\Omega$ ,  $Z_1 = Z_2 = (15 + j112.7)$ .

Main sliding surface parameters:  $k_{pq} = k_{pd} = 3.5$ ,  $k_{iq} = k_{id} = 0.7$ ,  $\eta_d = \eta_q = 15$ ,  $k = 50.2$ .

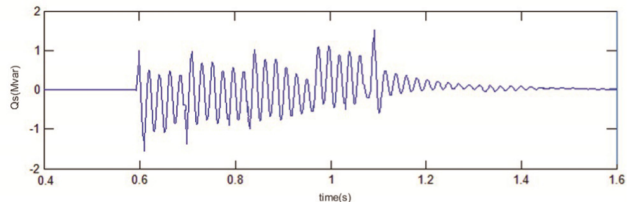
The simulation environment is set to: In order to trigger the system voltage spike, the capacitor is connected to the common bus in the wind farm during the simulation. Assuming that the capacitor is turned off when  $t = 0.6\text{s}$ , the capacitor



(a)



(b)



(c)

FIGURE 6. Simulation curve under conventional PI control strategy.

returns to normal operation when  $t = 1.1\text{s}$ , observe simulation results under conventional PI control and the improved control strategy. The simulation results are shown in the figure 6 and 7.

It can be seen from Fig. 6(a) that, after the conventional PI control strategy, the common bus voltage suddenly increases to 1.32 pu when the high voltage fault occurs. After the fault disappears, the bus voltage returns to normal. With the improved control strategy of this paper, the common bus voltage only jumps to 1.2 pu when the high voltage fault is triggered. After the fault disappears, the bus voltage returns to normal, as shown in Figure 7(a). It can be seen that the improved control strategy of this paper can effectively reduce the common bus voltage surge of about 0.12 pu by comparing the experimental data. It achieves better control results.

Figure 6(b) shows the curve of the DFIG rotor current after a high voltage fault is triggered under the conventional control strategy. Since the system is operating at the maximum wind energy tracking state, the rotor current hardly changes much. After adopting the improved control strategy of this paper, the DFIG rotor current curve is shown in Figure 7(b). After the fault occurs, the DFIG rotor current rapidly increases to 1.25 times, which makes the DFIG quickly emit reactive power and effectively suppresses the sudden rise in the common bus voltage.

Figure 6 (c) shows the curve of DFIG reactive power during system failure under traditional PI control strategy. Because the system is still in the state of maximum wind energy

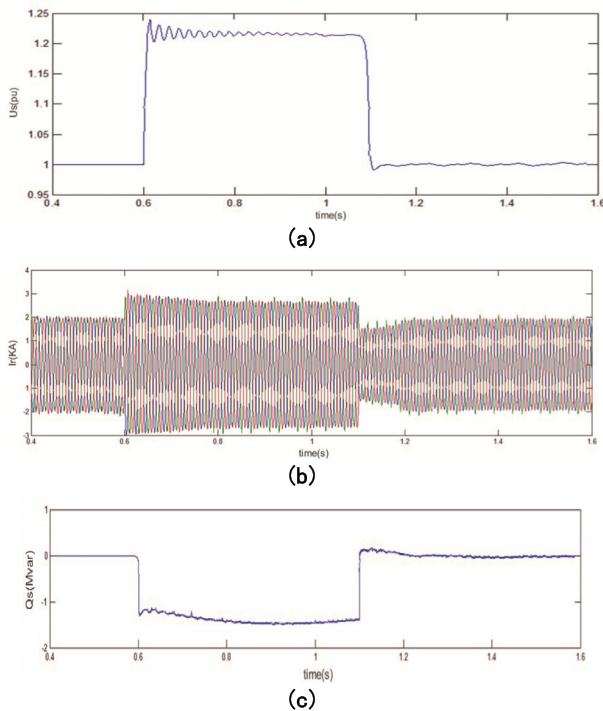


FIGURE 7. Improved simulation curve under control strategy.

tracking, the reactive power output from DFIG oscillates irregularly around the given value ‘0’. After the high voltage fault disappears, the reactive power output from DFIG tends to the given value ‘0’. As shown in Figure (7), the improved control strategy of this paper is adopted. When the system triggers a high voltage fault, the DFIG rotor current increases rapidly, which causes the DFIG to quickly emit reactive power. It effectively suppressing the sudden rise of the system voltage.

V. SYSTEM REAL-TIME SIMULATION EXPERIMENT VERIFICATION AND ANALYSIS

In order to verify the feasibility of the model engineering application, the single-machine DFIG control model was extended to the wind farm cluster control model, and the RTDS-based ‘magnetic flux chain additional control’ real-time simulation system was developed. The system experimental schematic diagram is shown in Figure 8. The main experimental parameters are the same as the off-line simulation experimental parameters.

During the experiment, the RTDS completes the real-time data acquisition of the wind farm and the system bus voltage, and transmits the data to the upper computer. After the DSP processes the data according to the set control algorithm, the control command is issued. The control signal passes through the optical fiber and the photoelectric conversion module. The specific control commands are assigned to the back-to-back converters of each DFIG in the wind farm, and finally a typical wind farm grid-connected feedback control system is formed, thereby realizing the real-time control of the wind farm grid-connected operation.

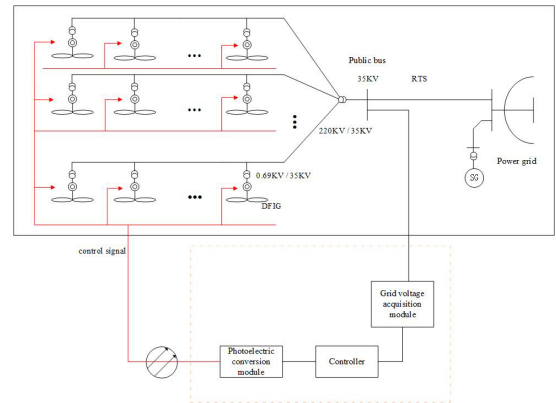


FIGURE 8. System experiment schematic.

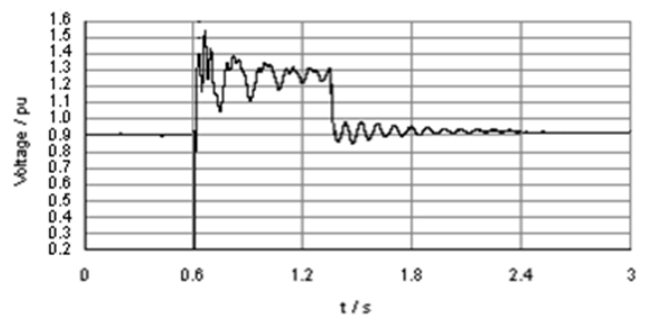


FIGURE 9. Conventional PI control common bus voltage response curve.

In the simulation, in order to achieve a sudden rise in the common bus voltage, the capacitor is connected at the common bus of the wind farm. When  $t=0.6s$ , the capacitor is turned off. When  $t=1.3s$ , the capacitor returns to normal operation. Observe simulation results under conventional PI control and the improved control strategy.

In the real-time simulation experiment, the grid voltage surge at the common busbar occurred at about  $t=0.6 s$ . Figure 9 and Figure 10 show the common bus voltage dynamic response curves when using the conventional PI control strategy and the joint additional control strategy. It can be seen from figure 9 that when the conventional PI control strategy is adopted, the common bus voltage burst is 0.47 pu during the system failure. After the fault disappears, the bus voltage returns to normal. As shown in Figure 10, the joint additional control strategy is adopted. When the high voltage fault is triggered, the common bus voltage burst is 0.25 pu. After the fault disappears, the bus voltage returns to normal.

Figure 11 and Figure 12 show the dynamic response curves of the rotor excitation current when the conventional PI control strategy and the joint additional control strategy are used. It can be seen from the figure that under the conventional control strategy, the DFIG rotor current hardly changes greatly after the high voltage fault is triggered. After adopting the joint additional control strategy, the DFIG rotor current rapidly increases to 1.5 times during the fault occurrence, which makes the DFIG quickly emit reactive power. It effectively suppresses the sudden rise of the common bus voltage.

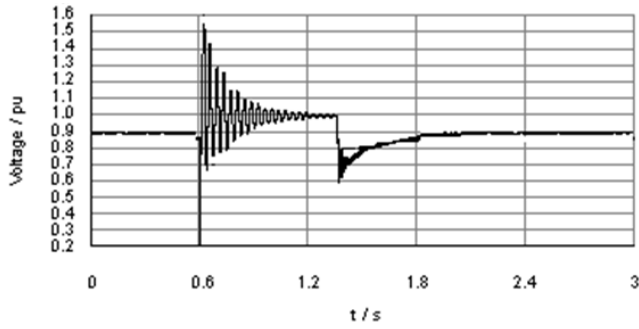


FIGURE 10. Joint additional control common bus voltage response curve.

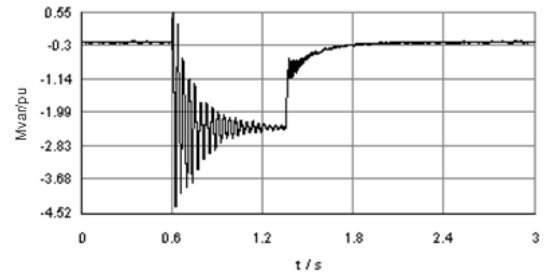


FIGURE 14. Magnetic flux chain additional control reactive power response curve.

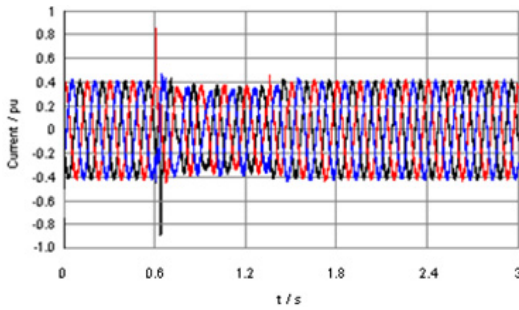
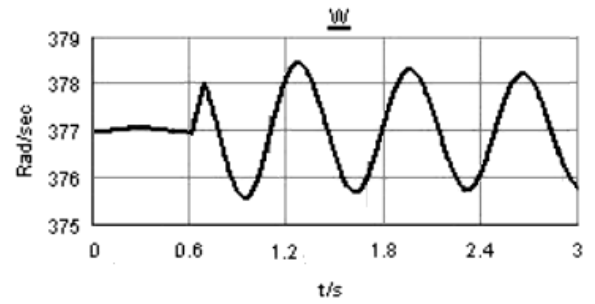


FIGURE 11. Conventional PI control rotor current response curve.



(a)

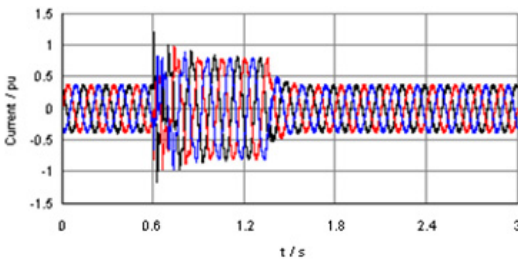
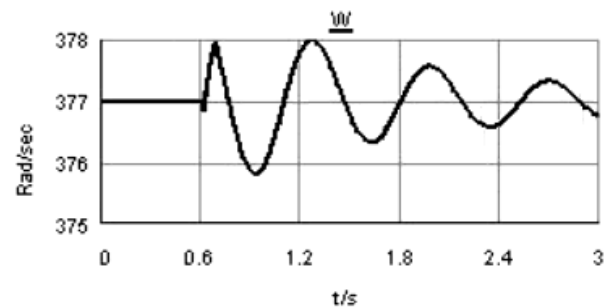


FIGURE 12. Flux linkage control rotor current response curve.



(b)

FIGURE 15. Synchronous generator speed.

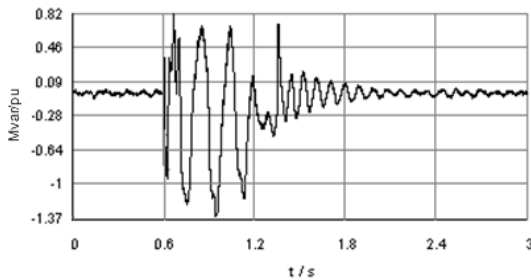


FIGURE 13. Conventional PI control reactive power response curve.

The experimental analysis results are highly consistent with the dynamic response curve of the rotor excitation current during off-line simulation.

Figure 13 and Figure 14 show the DFIG reactive power dynamic response curves when using the conventional PI control strategy and the joint additional control strategy. It can be seen from the figure that with the conventional PI control strategy, the reactive power of the doubly-fed fan output

violently oscillates during the fault. After the fault is eliminated, its reactive power tends to be stable. With the joint additional control strategy, the doubly-fed fan quickly outputs reactive power  $-2.41$  pu during the fault, and suppresses the high voltage. The experimental analysis results are consistent with the dynamic response curve of the fan reactive power during off-line simulation.

Figure (15) shows the speed change curve. Figure (a) shows the speed swing curve under normal control; Figure (b) shows the speed change curve under the joint control strategy. It can be seen from the comparison of the two figures that the rotor rocking curve decays faster after accessing the joint control strategy.

Figure (16) shows the active output curve. Figure (a) shows the real-time active output curve under normal control; Figure (b) shows the active output curve under joint control. Comparing the two figures, it can be seen that when the system has a high voltage, the system under the improved

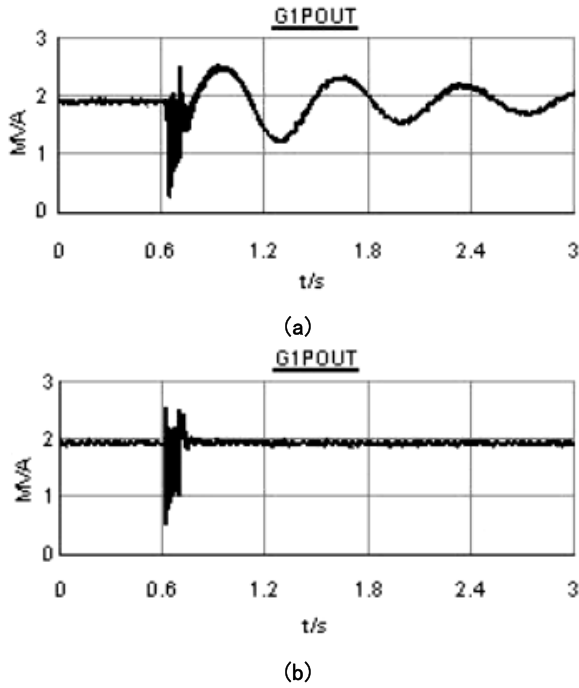


FIGURE 16. Active output power of doubly-fed wind turbine.

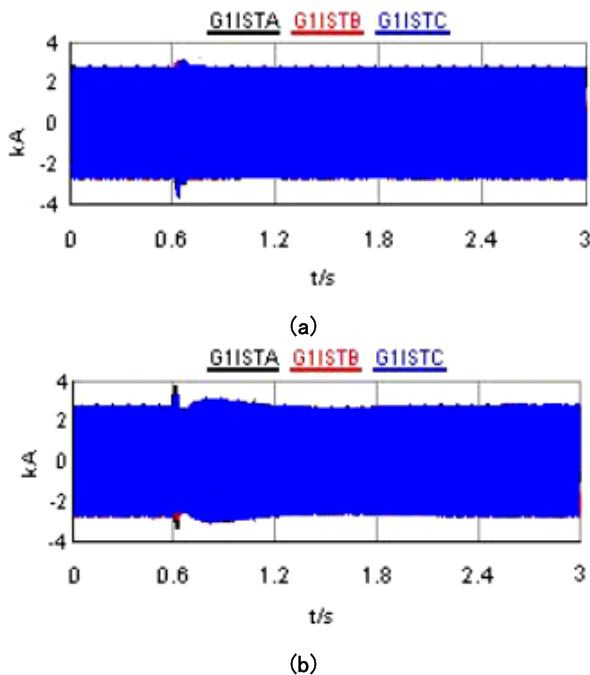


FIGURE 17. Stator current of doubly-fed generator.

control adjusts its reactive output so that the active output tends to be stable faster.

Figure (17) shows the stator current curve. Figure (a) shows the stator current variation curve under normal control; Figure (b) shows the stator current variation curve under improved control. Comparing the results of the above two cases, it can be seen that when the stator has a improved

control strategy, the instantaneous current increases, but it is not directly connected with the power electronic device, and the instantaneous current increase is still within the safe range. There is no negative impact on fans and systems.

### VI. ANALYSIS AND DISCUSSION OF SIMULATION RESULTS

This paper proposes a DFIG grid-connected rotor flux linkage control model based on structural decentralization theory. The system offline simulation experiment and system real-time simulation experiment were designed and analyzed, and the results were compared with the conventional PI control strategy.

First, an off-line simulation of the system’s improved control strategy and conventional PI control strategy was performed. In the simulation process, when the simulation time  $t=0.6s$ , disconnect the capacitor; when the simulation time  $t=1.1s$ , the capacitor is restored to normal operation. The simulation results are shown in Fig. 6 and 7. The results show that under the conventional PI control strategy, when a high voltage fault occurs, the common bus voltage suddenly increases to 1.32 pu, the rotor current is almost constant, and the output reactive power of DFIG occurs randomly around the given value. After the fault is completed, the bus voltage is restored to normal, the rotor current is unchanged, and the output reactive power of DFIG does not change much. Under the improved control strategy, when a high voltage fault occurs, the common bus voltage suddenly increases to 1.2 pu, the rotor current increases to 1.25 times, and the output reactive power of the DFIG increases rapidly. By contrast, the improved control strategy can effectively suppress the sudden rise of the system voltage.

Secondly, real-time simulation of the system’s improved control strategy and conventional PI control strategy was carried out. The simulation results are shown in Fig. 9-14. The results show that under the conventional PI control strategy, when a high voltage fault occurs, the common bus voltage suddenly increases to 0.47 pu, the rotor current is almost constant, and the output reactive power of the DFIG is maintained near the given value. Under the improved control strategy, when a high voltage fault occurs, the common bus voltage suddenly increases to 0.25 pu, the rotor current increases to 1.5 times, and the output reactive power of the DFIG rapidly increases to  $-2.41$  pu.

The real-time simulation results are consistent with the dynamic response of the offline simulation results. During grid high voltage faults, improved control strategy allows the system to quickly generate reactive power, which can effectively suppress high voltage faults and enhance system high voltage ride through capability. By comparing the speed change curves, it can be seen that the improved control strategy has significantly improved the stability of the system.

### VII. CONCLUSION

This paper mainly takes the grid-connected doubly-fed wind farm as the research object. It proposes an additional sliding

mode control strategy for the rotor flux adaptive terminal of doubly-fed wind farm aiming at improving the high voltage traversal performance of the 'wind-fire' hybrid transmission system. Compared with the traditional PI control method, when using an improved control strategy, the sudden increase in the common bus voltage in the offline simulation is reduced by 0.12 pu, and it is reduced by 0.22 pu under real-time simulation. And under this control strategy, the stator current of the off-line simulation is rapidly increased to 1.25 times, and the stator current is rapidly increased to 1.5 times during the real-time simulation. Therefore, the control strategy in this paper improves the support capacity of the common bus voltage. The dual-feed wind farm rotor flux adaptive terminal sliding mode additional control strategy can quickly send the reactive power during the high voltage fault of the power grid, delaying or even preventing the occurrence of overvoltage phenomenon has important theoretical reference significance for improving the power quality of the wind power generation system.

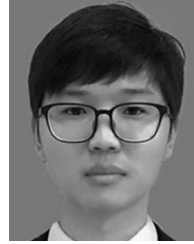
## REFERENCES

- [1] S. Luo and L. Zhu, "Research on control strategy of double feed converter under grid voltage soared," *Power Syst. Protection Control*, vol. 45, no. 24, pp. 123–129, Dec. 2017.
- [2] O. Nourelddeen and I. Hamdan, "A novel controllable crowbar based on fault type protection technique for DFIG wind energy conversion system using adaptive neuro-fuzzy inference system," *Protection Control Modern Power Syst.*, vol. 3, no. 1, Oct. 2018, Art. no. 35.
- [3] Y. E. Yanfei, W. Qi, and C. Ning, "Wind forecast model considering the characteristics of temporal and spatial distribution," *Power Syst. Protection Control*, vol. 45, no. 4, pp. 115–119, 2017.
- [4] M. Alsumiri, L. Li, L. Jiang, and W. Tang, "Residue theorem based soft sliding mode control for wind power generation systems," *Protection Control Mod. Power Syst.*, vol. 3, no. 1, p. 24, 2018.
- [5] S. Boubzizi, H. Abid, A. El Hajjaji, and M. Chaabane, "Comparative study of three types of controllers for DFIG in wind energy conversion system," *Protection Control Mod. Power Syst.*, vol. 3, no. 1, p. 21, 2018.
- [6] K. Chongqing and Y. Liangzhong, "Key scientific issues and theoretical research framework for power systems with high proportion of renewable energy," *Automat. Electr. Power Syst.*, vol. 41, no. 9, pp. 2–11, May 2017.
- [7] W. Shi, H. Bai, J. Qu, W. Wang, and Q. Huang, "Technology trend and development suggestions for wind power efficient utilization in China," *Eng. Sci.*, vol. 20, no. 3, pp. 51–57, Oct. 2018.
- [8] F. E. V. Taveiros, L. S. Barros, and F. B. Costa, "Heightened state-feedback predictive control for DFIG-based wind turbines to enhance its LVRT performance," *Int. J. Electr. Power Energy Syst.*, vol. 104, pp. 943–956, Jan. 2019.
- [9] K. Liao and L. Guofan, "Low voltage ride through technology control strategy for direct drive permanent magnet wind turbine converter," *J. Hunan Inst. Eng.*, vol. 28, no. 3, pp. 7–12, 2018.
- [10] C. Yang, X. Yang, and C. Tong, "An LVRT control strategy based on soft crowbar control for doubly fed induction wind power generations," *Proc. CSEE*, vol. 38, no. 8, pp. 2487–2495, Apr. 2018.
- [11] S. Lu, Z. Xu, L. Xiao, W. Jiang, and X. Bie, "Evaluation and enhancement of control strategies for VSC stations under weak grid strengths," *IEEE Trans. Power Syst.*, vol. 33, no. 2, pp. 1836–1847, Mar. 2018.
- [12] M. Kuzhali, S. J. Isac, and S. Poongothai, "Improvement of low voltage ride through capability of grid-connected DFIG WTs using fuzzy logic controller," in *Proc. Int. Conf. Intell. Comput. Appl.* Singapore: Springer, 2019, pp. 349–359.
- [13] Y. M. Alsmadi, L. Xu, F. Blaabjerg, A. J. P. Ortega, A. Y. Abdelaziz, A. Wang, and Z. Albatineh, "Detailed investigation and performance improvement of the dynamic behavior of grid-connected DFIG-based wind turbines under LVRT conditions," *IEEE Trans. Ind. Appl.*, vol. 54, no. 5, pp. 4795–4812, Sep./Oct. 2018.
- [14] S. G. Vennelaganti and N. R. Chaudhuri, "New insights into coupled frequency dynamics of AC grids in rectifier and inverter sides of LCC-HVDC interfacing DFIG-based wind farms," *IEEE Trans. Power Del.*, vol. 33, no. 4, pp. 1765–1776, Aug. 2018.
- [15] W. Li, G. Joos, and J. Belanger, "Real-time simulation of a wind turbine generator coupled with a battery supercapacitor energy storage system," *IEEE Trans. Ind. Electron.*, vol. 57, no. 4, pp. 1137–1145, Apr. 2010.
- [16] S. Ghosh and S. Kamalasan, "An energy function-based optimal control strategy for output stabilization of integrated DFIG-flywheel energy storage system," *IEEE Trans. Smart Grid*, vol. 8, no. 4, pp. 1922–1931, Jul. 2017.
- [17] M. K. Döşoğlu, "Enhancement of SDRU and RCC for low voltage ride through capability in DFIG based wind farm," *Elect. Eng.*, vol. 99, no. 2, pp. 673–683, Jun. 2017.
- [18] M. Kalantar and S. M. Mousavi, "Dynamic behavior of a stand-alone hybrid power generation system of wind turbine, microturbine, solar array and battery storage," *Appl. Energy*, vol. 87, no. 10, pp. 3051–3064, 2010.
- [19] M. K. Döşoğlu, "A new approach for low voltage ride through capability in DFIG based wind farm," *Int. J. Electr. Power Energy Syst.*, vol. 83, pp. 251–258, Dec. 2016.
- [20] M. Rahimi and M. Parniani, "Coordinated control approaches for low-voltage ride-through enhancement in wind turbines with doubly fed induction generators," *IEEE Trans. Energy Convers.*, vol. 25, no. 3, pp. 873–883, Sep. 2010.
- [21] M. K. Döşoğlu, "Hybrid low voltage ride through enhancement for transient stability capability in wind farms," *Int. J. Electr. Power Energy Syst.*, vol. 78, pp. 655–662, Jun. 2016.
- [22] M. Rahimi and M. Parniani, "Low voltage ride-through capability improvement of DFIG-based wind turbines under unbalanced voltage dips," *Int. J. Electr. Power Energy Syst.*, vol. 60, pp. 82–95, Sep. 2014.
- [23] M. K. Döşoğlu, "Nonlinear dynamic modeling for fault ride-through capability of DFIG-based wind farm," *Nonlinear Dyn.*, vol. 89, no. 4, pp. 2683–2694, Sep. 2017.
- [24] M. Q. Duong, A. Dolara, F. Grimaccia, S. Leva, M. Mussetta, and G. Sava, "Fault ride-through capability and damping improvement In DFIG," *Tech. Rep.*, 2016, pp. 241–252.
- [25] K. Vinothkumar and M. P. Selvan, "2010 IEEE international conference on sustainable energy technologies (ICSET) : 6-9 December 2010, Kandy, Sri Lanka," in *Proc. IEEE Int. Conf. Sustain. Energy Technol. (ICSET)*, 2010, pp. 1–5.
- [26] M. Q. Duong, G. N. Sava, F. Grimaccia, S. Leva, M. Mussetta, S. Costinas, and N. Golovanov, "Improved LVRT based on coordination control of active crowbar and reactive power for doubly fed induction generators," in *Proc. 9th Int. Symp. Adv. Topics Electr. Eng.*, May 2015, pp. 650–655.
- [27] F. Zhang, W. E. Leithea, and O. Anaya-Lara, "Wind turbine control design to enhance the fault ride-through capability," in *Proc. IET Conf. Renew. Power Gener.*, Sep. 2011, pp. 1–6.
- [28] E. Muljadi, C. P. Butterfield, B. Parsons, and A. Ellis, "Effect of variable speed wind turbine generator on stability of a weak grid," *IEEE Trans. Energy Convers.*, vol. 22, no. 1, pp. 29–36, Mar. 2007.
- [29] W. Tang, J. Hu, Y. Chang, and F. Liu, "Modeling of DFIG-based wind turbine for power system transient response analysis in rotor speed control timescale," *IEEE Trans. Power Syst.*, vol. 33, no. 6, pp. 6795–6805, Nov. 2018.
- [30] K. Givaki, D. Chen, and L. Xu, "Current error based compensations for VSC current control in weak grids for wind farm applications," *IEEE Trans. Sustain. Energy*, vol. 10, no. 1, pp. 26–35, Jan. 2019.
- [31] Y. M. Alsmadi, L. Xu, F. Blaabjerg, A. P. Ortega, and A. Wang, "Comprehensive analysis of the dynamic behavior of grid-connected DFIG-based wind turbines under LVRT conditions," in *Proc. IEEE Energy Convers. Congr. Expo.*, Sep. 2015, pp. 4178–4187.
- [32] F. Golnary and H. Moradi, "Design and comparison of quasi continuous sliding mode control with feedback linearization for a large scale wind turbine with wind speed estimation," *Renew. Energy*, vol. 127, pp. 495–508, Nov. 2018.
- [33] G. Abad, J. Lopez, M. Rodriguez, L. Marroyo, and G. Iwanski, *Doubly Fed Induction Machine: Modeling and Control for Wind Energy Generation*. Beijing, China: China Machine Press, 2014.



**XINYU LIU** was born in Henan, China, in 1976. He received the master's and Ph.D. degrees from Zhengzhou University, China.

Since 2004, he has been with the North China University of Water Resources and Electric Power, where he is currently an Associate Professor and a Master Tutor. He is the author of two books. He received the third prize of Henan Science and Technology Progress Award and the second prize of Henan Province Information Technology Education Outstanding Achievement Award. In 2016, he was named Young Backbone Teacher of Henan colleges and universities.



**DONGHONG JIAO** was born in July 1990. He is currently a Master with the North China University of Water Resources and Electric Power. His main research interest includes research on joint optimization controller for grid-connected high and low voltage crossing of large-scale doubly fed wind farms.

...



**XIANWEI LI** was born in September 1994. He is currently a Master with the North China University of Water Resources and Electric Power. His main research interest includes the control strategy of converters with double-fed wind power grid-connected.